Population connective field modeling reveals retinotopic visual cortex organization in the prenatal human brain

So-Hyeon Yoo[1], Anne-Sophie Kieslinger[1] and Michael A. Skeide[1] ✉

[1] Research Group Learning in Early Childhood,
Max Planck Institute for Human Cognitive and Brain Sciences,
Stephanstraße 1A, 04103 Leipzig, Germany

✉ e-mail: skeide@cbs.mpg.de

Correspondence should be addressed to Michael A. Skeide

Abstract

The visual space is sampled by cortical field maps in which nearby neuronal populations encode nearby locations of images received from the retina. Whether this retinotopic cortical organization already emerges in the prenatal human brain before visual experience is currently unknown. To answer this question in vivo, we applied population connective field modeling to 526 functional magnetic resonance imaging datasets ranging from prenatal to young adult age. We found retinotopically organized eccentricity and polar angle connectivity maps in V2 of the visual cortex as early as in the 21st week of gestation while connective field model fits increased significantly throughout development. These results highlight that retinotopic cortical maps develop in the second trimester of pregnancy, predating visual experience.

Introduction

Visual cortices transform input signals from the retina into internal representations of the visual space providing the foundation for perceiving and interpreting environments[1]. These cortices are organized retinotopically, such that nearby locations of the retinal image are encoded by nearby neuronal populations[2,3]. In a retinotopic map, nearby neuronal populations encode eccentricity, that is, the distance from the center of the visual space. Specifically, the surface area representing visual space decreases with increasing eccentricity towards anterolateral visual cortices[4–7]. Moreover, nearby neuronal populations encode polar angle, that is, the angular distance between a location in visual space relative to an axis, like the horizontal median. Polar angle reversal from ascending to descending progression at the boundary between V1 and V2 of the visual cortex is considered as a critical feature of retinotopic organization[5–7].

While retinotopic visual cortex organization has been extensively studied in the adult brain its emergence in the developing brain remains hardly understood[1]. Functional magnetic resonance imaging (fMRI) studies show that, by the age of 5 years, eccentricity and polar angle maps are qualitatively similar to adults[8,9]. In macaque monkeys, however, retinotopically organized eccentricity and polar angle maps have been identified already at a neonatal age using fMRI[10]. Other retinotopic features, including response preferences for horizontal and vertical orientation as well as high and low spatial frequencies have been revealed by fMRI in infants aged 5 months[11]. Whether retinotopic organization is present in neonatal, let alone prenatal humans, is currently unknown.

To answer this question, we applied population connective field modeling to 526 resting-state fMRI datasets from developmental branches of the Human Connectome Project[12,13]. Population connective field modeling was employed here to detect vertices in V1 that best predict hemodynamic responses of vertices in V2 based on cortical surface templates of these regions of interest including

their eccentricity and polar angle values[14–17]. Following nonhuman primate work, we hypothesized that retinotopically organized eccentricity and polar angle connectivity maps can be identified at a neonatal age at the latest[10]. At the same time, we hypothesized that connective field model fits increase significantly in the course of further pre- and postnatal brain development.

We consistently found retinotopically organized eccentricity and polar angle connectivity maps from prenatal age onwards, as early as in the 21st week of gestation. In line with our hypothesis, connective field model fits turned out to increase significantly from prenatal to adult age.

Results

Group characteristics

Prenatal data including fetal MRI scans recorded during the second trimester of pregnancy (here between 21 and 28 weeks gestational age) and the third trimester of pregnancy (≥29 weeks gestational age) were compared against preterm neonatal data (born <37 weeks gestational age) and full-term neonatal data (born ≥37 weeks gestational age) as well as MRI scans recorded during adolescence (12–17 years) and early adulthood (18–21 years). All six groups comprise cross-sectional data of different subjects (Table 1).

Average standardized temporal derivatives of time courses based on root-mean-squared variance over vertices was less than 1 for all subjects indicating effective head motion correction in all groups (left hemisphere: second trimester: 0.896 ± 0.08, third trimester: 0.912 ± 0.085, preterm neonates: 0.984 ± 0.030, full-term neonates: 0.973 ± 0.040, adolescents: 0.997 ± 0.001, adults: 0.997 ± 0.001; right hemisphere: second trimester: 0.895 ± 0.081, third trimester: 0.912 ± 0.085, preterm neonates: 0.985 ± 0.030, full-term neonates: 0.980 ±0.037, adolescents: 0.997 ± 0.001, adults: 0.997 ± 0.001).

Table 1 | Group characteristics.

	tri-2[2] prenatal	tri-3[3] prenatal	preterm neonatal	full-term neonatal	adolescent	adult
mean scan age	26.08	32.24[4]	38.6[4]	41.37[4]	14.49[5]	20.21[5]
scan age range	21–28	29–36[4]	34–44[4]	37–44[4]	12–17[5]	18–21[5]
sex (f/m)[1]	na	na	30/35	53/73	45/26	32/22
n subjects	109	101	65	126	71	54

[1]female/male [2/3]second/third trimester of pregnancy [4]age in weeks [5]age in years

Population connective field model fitting

Hemodynamic time courses predicted by the population connective field model in V1 of the visual cortex were correlated with observed hemodynamic time courses measured in a dorsal and a ventral region of interest in V2 of the left and right visual cortex[16]. The model explained up to 47% of the variance in the measured data. Median correlation coefficients for each group in both hemispheres were: $r = 0.16$ in the second trimester, $r = 0.17$ in the third trimester, $r = 0.14$ in preterm neonates, $r = 0.21$ in full-term neonates, $r = 0.37$ in adolescents and $r = 0.38$ in adults. Bootstrapped Kruskal-Wallis tests on the distribution of above-threshold correlation coefficients revealed large and statistically significant differences between groups (left hemisphere: $\chi^2(5) = 187329.11$, effect size $\eta^2 = 0.47$, $p < 0.001$; right hemisphere: $\chi^2(5) = 203619.15$, effect size $\eta^2 = 0.47$, $p < 0.001$) (see Supplementary Table S1 for post-hoc subgroup comparisons). The distribution of connective field size estimates also differed significantly between groups (left hemisphere: $\chi^2(5) = 103552.61$, effect size $\eta^2 = 0.35$, $p < 0.001$; right hemisphere: $\chi^2(5) = 107908.92$, effect size $\eta^2 = 0.34$, $p < 0.001$) (see Supplementary Table S2 for post-hoc subgroup comparisons).

Eccentricity connectivity mapping

Eccentricity estimates obtained from the empirical data were first compared with a model of local spatial correlations based on simulated random hemodynamic time courses across the entire cortical surface. In all groups, the connective field model applied to the empirical data fit Benson's eccentricity template better than the simulated data in both hemispheres, as indicated by empirical and simulated mean squared differences (eMSD vs. sMSD) (second trimester: eMSD = 28.03 and sMSD = 54.73, z = -9.05, effect size r = -0.87, $p < 0.001$, third trimester: eMSD = 29.72 and sMSD = 45.95, z = –8.58, effect size r = -0.85, $p < 0.001$, preterm neonates: eMSD = 22.56 and sMSD = 42.14, z = -6.96, effect size r = -0.86, $p < 0.001$, full-term neonates: eMSD = 19.98 and sMSD =41.89, z = -9.05, effect size r = 0.86, $p < 0.001$, adolescents: eMSD = 6.97 and sMSD = 33.38, z = -7.32, effect size r = -0.87, $p < 0.001$, adults: eMSD =7.75 and sMSD = 30.91, z = -6.39, effect size r =-0.87, $p < 0.001$)[15]. Surface mapping revealed that eccentricity estimates increased towards anterolateral V2 (Fig.1). Bootstrapped Kruskal-Wallis tests indicated small but significant group differences (left hemisphere: $\chi^2(5) = 781.79$, effect size $\eta^2 = 0.03$, $p < 0.001$; right hemisphere: $\chi^2(5) = 2706.39$, effect size $\eta^2 = 0.05$, $p < 0.001$) (see Supplementary Table S3 for post-hoc subgroup comparisons).

Polar angle connectivity mapping

Polar angle estimates obtained from the empirical data were first compared with a model of local spatial correlations based on simulated random hemodynamic time courses across the entire cortical surface. In all groups, the connective field model applied to the empirical data fit Benson's polar angle template better than the simulated data in both hemispheres, as indicated by empirical and simulated mean squared differences (eMSD vs. sMSD) (second trimester: eMSD = 2907.56 and sMSD = 9555.30, z = -9.06, effect size r = -0.87, $p < 0.001$, third trimester: eMSD = 3273.59 and sMSD = 8005.15, z = -8.72, effect size r = -0.87, $p < 0.001$, preterm neonates: eMSD = 2644.30 and sMSD = 7545.84, z = -7.01, effect

size r = -0.87, $p < 0.001$, full-term neonates: eMSD = 2860.51 and sMSD =7417.98, z = -9.74, effect size r = -0.87, $p < 0.001$, adolescents: eMSD = 1782.98 and sMSD = 7797.53, z = -7.32, effect size r = -0.87, $p < 0.001$, adults: eMSD = 2167.82 and sMSD = 7458.89, z = -6.38, effect size r = -0.87, $p < 0.001$)[15]. Surface mapping revealed that, at the boundary between V1 and V2, polar angle estimates reversed from ascending to descending progression (Fig.2). Bootstrapped Kruskal-Wallis tests indicated medium and significant group differences (left hemisphere: $\chi^2(5) = 7084.11$, effect size $\eta^2 = 0.09$, $p < 0.001$; right hemisphere: $\chi^2(5) = 7411.15$, effect size $\eta^2 = 0.09$, $p < 0.001$) (see Supplementary Table S4 for post-hoc subgroup comparisons).

Gradients computed at each vertex in a right-to-left, anterior-to-posterior and dorsal-to-ventral coordinate system confirmed that polar angle estimates increased in ventral direction in all groups (Fig.3) (see Supplementary Table S5 for averaged gradient results) but nevertheless differed significantly between groups (left hemisphere V2 ventral: right direction: $\chi^2(5) = 29.93$, effect size $\eta^2 = 0.24$, $p < 0.001$, anterior direction: $\chi^2(5) = 90.11$, effect size $\eta^2 = 0.41$, $p < 0.001$, dorsal direction: $\chi^2(5) = 93.33$, effect size $\eta^2 = 0.42$, $p < 0.001$; left hemisphere V2 dorsal: right direction: $\chi^2(5) = 7.82$, effect size $\eta^2 = 0.12$, $p = 0.16$, anterior direction: $\chi^2(5) = 45.43$, effect size $\eta^2 = 0.29$, $p < 0.001$, dorsal direction: $\chi^2(5) = 49.01$, effect size $\eta^2 = 0.31$, $p < 0.001$; right hemisphere V2 ventral: right direction: $\chi^2(5) = 55.61$, effect size $\eta^2 = 0.33$, $p < 0.001$, anterior direction: $\chi^2(5) = 61.79$, effect size $\eta^2 = 0.34$, $p < 0.001$, dorsal direction: $\chi^2(5) = 79.13$, effect size $\eta^2 = 0.39$, $p < 0.001$; right hemisphere V2 dorsal: right direction: $\chi^2(5) = 32.95$, effect size $\eta^2 = 0.25$, $p < 0.001$, anterior direction: $\chi^2(5) = 69.60$, effect size $\eta^2 = 0.36$, $p < 0.001$, dorsal direction: $\chi^2(5) = 40.99$, effect size $\eta^2 = 0.28$, $p < 0.001$).

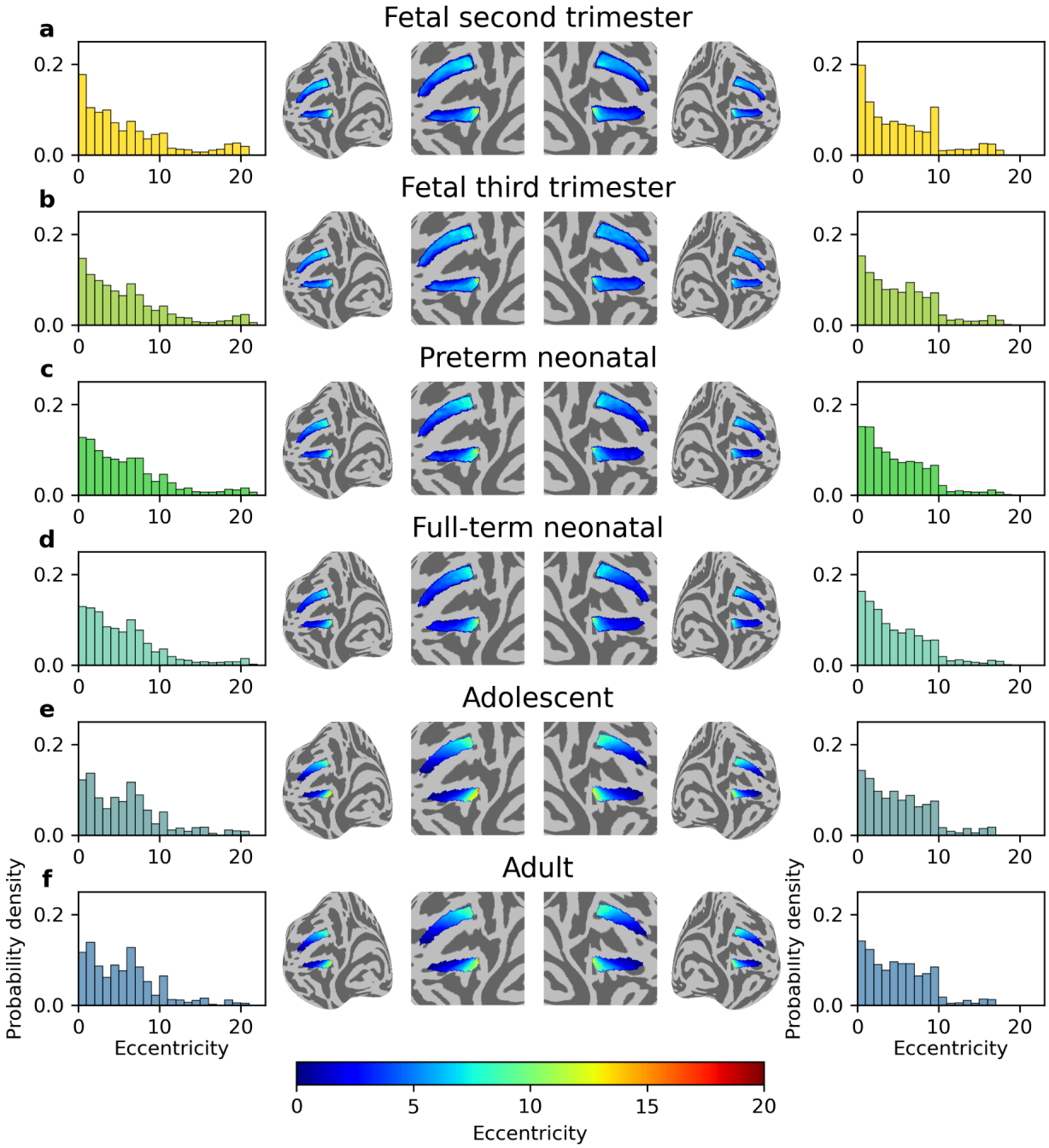

Fig. 1 | Eccentricity connectivity maps. a, Fetal second trimester. **b**, Fetal third trimester. **c**, Preterm neonatal. **d**, Full-term neonatal. **e**, Adolescent. **f**, Adult. Maps are averaged within each group. A value of 0 is assigned to vertices at the boundaries of each region of interest in which the connective field was not estimated. The color bar indicates eccentricity estimates (degrees from the fovea). Histograms include dorsal and ventral regions of interest. x-axes depict eccentricity estimates and y-axes depict probability density distributions.

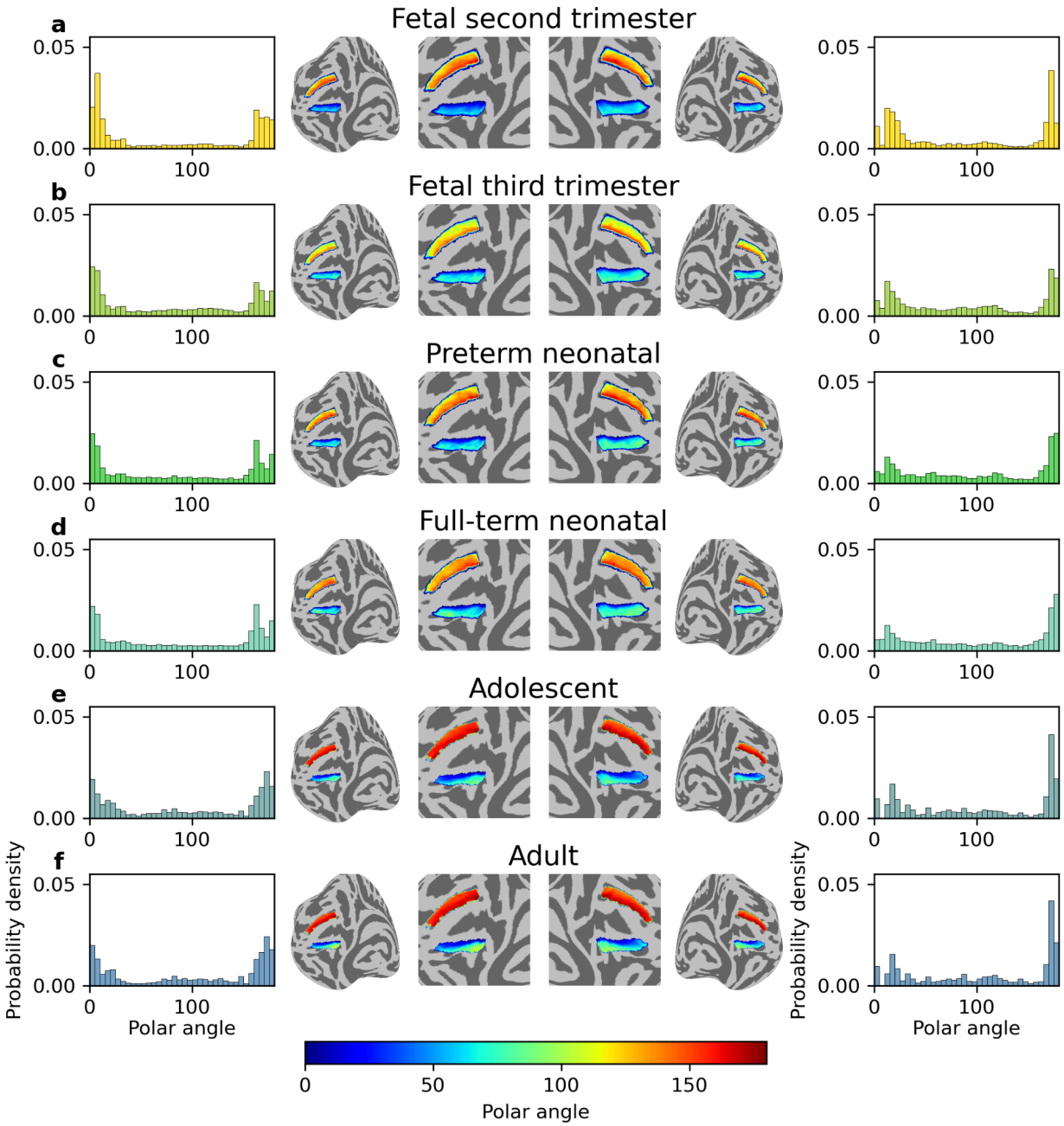

Fig. 2 | Polar angle connectivity maps. a, Fetal second trimester. **b**, Fetal third trimester. **c**, Preterm neonatal. **d**, Full-term neonatal. **e**, Adolescent. **f**, Adult. Maps are averaged within each group. A value of 0 is assigned to vertices at the boundaries of each region of interest in which the connective field was not estimated. The color bar indicates polar angle estimates (angular distance from the horizontal median in degrees). Histograms include dorsal and ventral regions of interest. x-axes depict polar angle estimates and y-axes depict probability density distributions.

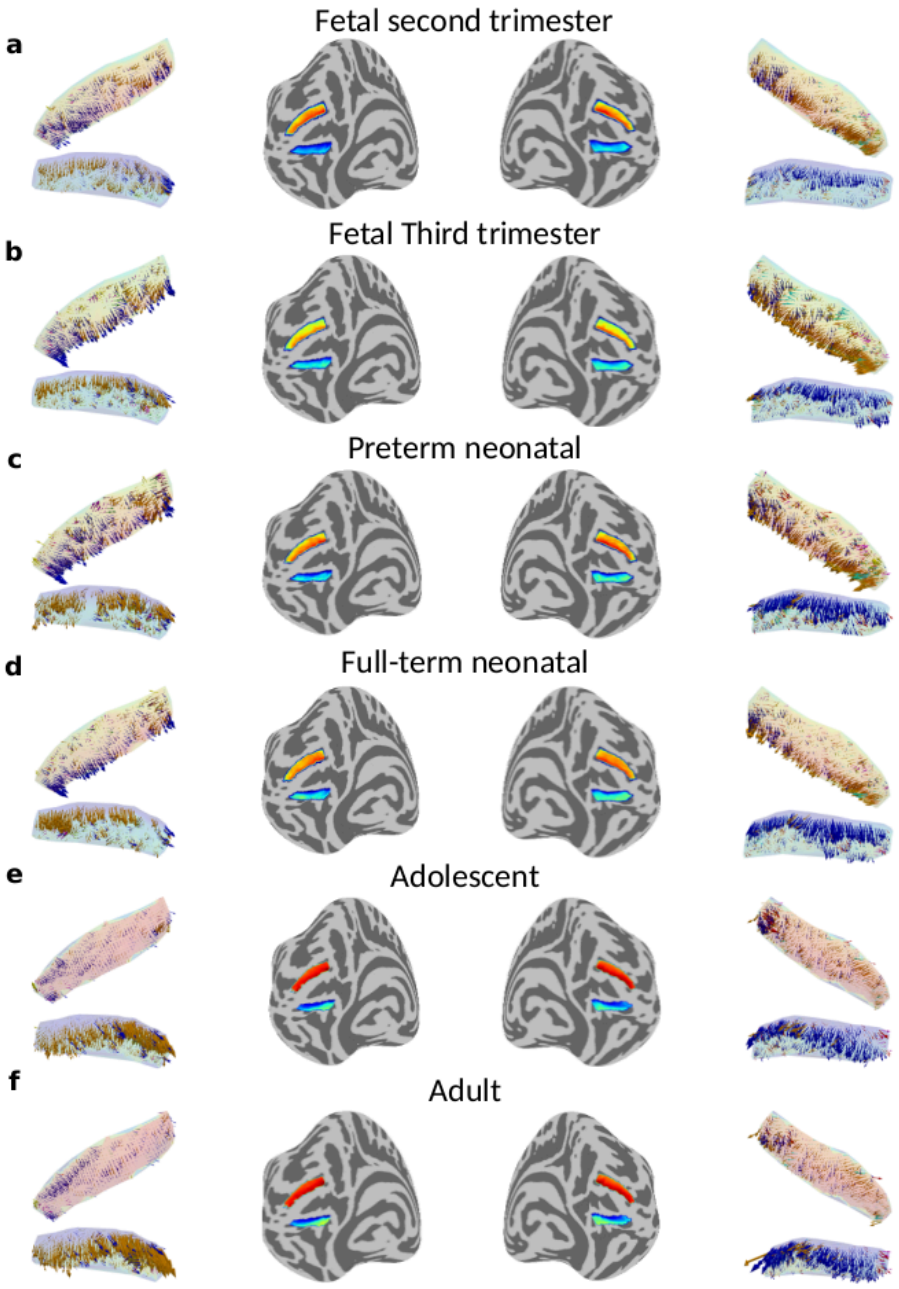

Fig. 3 | Polar angle gradient maps. a, Fetal second trimester. **b**, Fetal third trimester. **c**, Preterm neonatal. **d**, Full-term neonatal. **e**, Adolescent. **f**, Adult. First and fourth column: Gradient maps averaged within each group. Second and third column: polar angle connectivity maps from Fig. 2. Directions and colors of the arrows indicate the direction of gradients. Sizes of the arrows indicate the magnitude of gradients.

Discussion

Population connective field modeling of fMRI data revealed a retinotopic organization of visual cortices in prenatal human brains. Already in the 21st gestational week, eccentricity estimates increased towards anterolateral V2 of the visual cortex and polar angle estimates reversed from ascending to descending progression at the boundary between V1 and V2. At the same time, correlations between hemodynamic time courses predicted by the model and hemodynamic time courses observed in the data increased significantly from prenatal to adult age.

Retinotopic human visual cortex organization in the second trimester of pregnancy is remarkable from a behavioral perspective since the eyes typically open only by 28 weeks of gestation, pupils constrict and dilate only at around 31 weeks of gestation, and the fetus orients to external laser light stimuli only by around 34 weeks of gestation[18,19]. Furthermore, from an environmental perspective, biophysical modeling results suggest that intrauterine illumination is severely limited by maternal tissue[20]. From a neuroscience perspective, however, the results reported here can be explained by animal models based on the observation that spontaneous stimulus-independent neural activity is necessary for the development of visual receptive field properties related to retinotopic maps. Spontaneous neural activity is thought to weaken or eliminate imprecise synaptic connections while strengthening and maintaining correctly targeted connections. This neuroplastic refinement process can be completed in animals well before behavioral signs of visual processing emerge and even before photoreceptors respond to light[21–24]. How these findings translate to the developing human brain is not known yet. Future studies using longitudinal high-field MRI might be able to shed light on these processes at a mesoscopic scale capturing layer-specific hemodynamic responses and fiber projections in vivo and noninvasively.

The correspondence between the population connective field model and the measured hemodynamic responses was highest in young adults supporting the interpretation that retinotopic organization is most pronounced in the fully developed brain. Correspondence was significantly but only slightly larger compared to adolescents suggesting little retinotopic refinement after childhood. This finding is in line with previous work[8,9] but does not exclude changes at later developmental stages, such as increasingly more V1 surface area representing the lower than the upper vertical meridian of the visual space during task-based functional MRI[25].

Connective field model fits increased gradually and significantly from the 21st week of gestation to the neonatal age. The preterm neonate group emerged as an outlier in this developmental trajectory since their median correlation coefficients were the lowest of the entire sample, even slightly but significantly below those of the second trimester prenatal group. Follow-up MRI work is needed to find out whether this difference relates to known maturational risk factors associated with preterm birth, such as reduced fractional anisotropy and neurite density[26].

It is plausible to assume that the developmental increase in retinotopic organization reported here relates to a similar developmental increase in precision of neural connectivity between V1 and V2 of the visual cortex[24]. However, contributions of other factors beyond our experimental control, such as more noisy and variable signals in the developing brain, remain to be ruled out in future investigations[27,28].

Methods

Participants

Prenatal and neonatal participants. Prenatal and neonatal participants were recruited between 2015 and 2019 at St Thomas' Hospital in London for the Developing Human Connectome Project. Written informed consent of all legal guardians was obtained for all participants prior to taking part in the study. All study procedures were reviewed and approved by the London—Riverside Research Ethics Committee of the Health Research Agency (REC: 14/Lo/1169)[13,29]. The analysis of the pre-existing data was approved by the Ethics Committee at the Medical Faculty of the University of Leipzig, Germany (IRB00001750).

110 unique prenatal datasets corresponding to the second trimester of pregnancy (between 21 and 28 weeks gestational age) and 105 unique prenatal datasets corresponding to the third trimester of pregnancy (≥29 weeks gestational age) were included in the current study (mean gestational age 32.39 weeks, range 29–38.29 weeks). Additionally, we included 65 preterm neonates born <37 weeks gestational age (mean gestational age 31.92 weeks, range 23–36 weeks). 27 neonates admitted to neonatal intensive care, nine neonates with incomplete or abandoned scans, one neonate with vermian hypoplasia and one neonate with congenital heart disease were excluded from the study. The final cohort of 126 full-term neonates born ≥37 weeks gestational age (mean gestational age 39.98 weeks, range 37–42 weeks) had normal findings on clinical examination by a neonatologist prior to MRI data acquisition. Neuroradiological inspection of the MRI data mostly revealed clinically insignificant incidental findings[30]. Regardless of a potential clinical significance, incidental findings with unlikely measurable relevance for functional connectivity analysis were permissible[29].

Adolescent and adult participants. Adolescent and adult participants were recruited between 2017 and 2019 in Boston, Los Angeles, Minneapolis and St. Louis for the Human Connectome

Project – Development. Written informed consent of all legal guardians was obtained for all participants prior to taking part in the study. All study procedures were reviewed and approved by a central institutional review board at Washington University in St. Louis. The analysis of the pre-existing data was approved by the Ethics Committee at the Medical Faculty of the University of Leipzig, Germany (IRB00001750).

125 unique datasets were included in the current study and grouped into adolescence (mean scan age 14.49 years, range 12–17 years) and early adulthood (mean scan age 20.21 years, range 18–21 years). 289 datasets that did not pass the quality control procedure were excluded from our analysis (see Data Preprocessing below). We also excluded 34 subjects with visual impairments. Neuroradiological inspection of the MRI data revealed no clinically significant incidental findings

Data acquisition

Prenatal and neonatal data. Prenatal and neonatal images were collected on a 3T Philips Achieva scanner with a neonatal 32-channel phased-array head coil at the Evelina London Children's Hospital. These data are publicly available as part of the fourth release of the Developing Human Connectome Project (https://biomedia.github.io/dHCP-release-notes/) and were accessed in the National Institute of Mental Health Data Archive (NDA)[13].

Neonates were scanned without sedation during natural sleep following feeding and swaddling in a vacuum-evacuated blanket. To standardize pose, subjects were placed on a cradle. Hearing protection was provided in the form of molded dental putty, Minimuffs on-ear noise attenuators and an acoustic hood[31].

For structural imaging, a T2-weighted fast spin echo image was acquired twice with TR = 12 s, TE = 156 ms, SENSE factor: axial = 2.11 and sagittal = 2.58, 290 × 290 × 203 voxels, voxel size 0.8 mm x

0.8 mm x 1.6 mm (overlapped by 0.8 mm). In addition, a T1-weighted inversion recovery fast spin echo image was acquired twice with TR = 4,795 ms, TE = 8.7 ms, SENSE factor: axial = 2.26 and sagittal = 2.66 and matched to the T2-weighted image in terms of number of voxels and voxel size[32].

For functional imaging, 2,300 T2*-weighted single-shot echo-planar imaging volumes were acquired with TR = 392 ms, TE = 38 ms, flip angle = 34°, multiband acceleration factor of 9, 67 × 67 × 45 voxels, voxel size 2.15 mm x 2.15 mm x 2.15 mm. Single-band reference scans were also acquired with bandwidth-matched readout, along with additional spin-echo echo-planar imaging acquisitions (fieldmaps) with 4 x AP and 4 x PA phase-encoding directions[32].

Adolescent and adult data. Adolescent and adult data were collected on 3T Siemens Prisma scanners with 32-channel head coils at Harvard University, University of California at Los Angeles, University of Minnesota, and Washington University in St. Louis. These data are publicly available as part of the second release of the Human Connectome Project – Development and were accessed in the National Institute of Mental Health Data Archive (NDA)[12].

For structural imaging, a T2-weighted variable-flip-angle turbo-spin-echo image was acquired with TR = 3,200 ms, TE = 564 ms, 320×300×208 voxels, voxel size 0.8 mm x 0.8 mm x 0.8 mm). In addition, a T1-weighted multi-echo image was acquired twice with TR = 2,500 ms, TE1 = 1.81 ms, TE2 = 3.6 ms, TE3 = 5.39 ms, TE 4 = 7.18 ms and matched to the T2-weighted image in terms of number of voxels and voxel size. Subjects watched a movie during these procedures[33].

For functional imaging, 488 T2*-weighted single-shot echo-planar imaging volumes were acquired four to six times with TR = 800 ms, TE = 37 ms, flip angle = 52°, multiband acceleration factor of 8, 67 × 67 × 45 voxels, voxel size 2 mm x 2 mm x 2 mm. Subjects were instructed to look at a fixation cross during this procedure. A single-band spin-echo echo-planar imaging fieldmap with one AP and one PA phase-encoding direction was also acquired with bandwidth-matched readout[33].

Data preprocessing

Developing Human Connectome Project: Prenatal and neonatal images

Structural image preprocessing. T2-weighted structural images were pre-processed according to the structural pipeline developed in the developing human connectome project (dHCP)[34]. First, motion correction and super-resolution reconstruction techniques were employed on T1- and T2-weighted structural images[35,36]. Second, the reconstructed T1- and T2-weighted images were bias-corrected using the N4 bias field correction algorithm[37] and the Brain Extraction Tool (BET) implemented in the FSL software package (5.0.11)[38]. Finally, each T1-weighted image was registered rigidly to the corresponding T2-weighted image using the Medical Image Registration ToolKit (MIRTK).

After preprocessing, the T2-weighted images were segmented into different tissue types (white matter, cortical gray matter, subcortical gray matter, and cerebrospinal fluid) using the Developing brain region annotation with Expectation-Maximization (Draw-EM) algorithm[39]. Draw-EM was also employed to generate surface meshes (white matter, pial, and mid-thickness surfaces). For further analysis, the number of vertices in the white and pial meshes should be equal. Only those datasets that exhibited an identical number of vertices in the white matter and pial meshes following the reconstruction of surface data were subjected to further analysis. This step is necessary since when resampling a volume image to a surface image, the signals of multiple voxels in a triangle connecting each vertex in the meshes are restructured into a single time series. Accordingly, if the number of vertices in white matter and pial meshes are different, image distortion occurs and resampling accuracy decreases.

Functional image preprocessing. T2*-weighted functional images were preprocessed in accordance with the resting-state functional processing pipeline in the dHCP[32]. First, local signal

distortions resulting from magnetic field inhomogeneities were corrected using the FSL TOPUP tool[40]. Second, slice-to-volume and rigid-body realignment were employed using the FSL EDDY tool[41] to correct for in- and out-of-volume head motion and dynamic distortions. Finally, residual head motion, motion artifacts arising from multiband acceleration, and physiological noise were removed using a linear regression model implemented in FMRIB's ICA-based Xnoiseifier tool (FIX, v1.066)[42].

Human Connectome Project: Adolescent and adult images

Structural image preprocessing. T1- and T2-weighted structural images were preprocessed according to the structural pipeline of the Human Connectome Project (HCP-D). This pipeline comprises three preprocessing stages: PreFreeSurfer, FreeSurfer and PostFreeSurfer. In PreFreeSurfer, structural images are distortion-corrected, aligned, and registered to the Montreal Neurological Institute (MNI) standard space using the FMRIB software library implemented in FSL. In FreeSurfer, structural cortical maps are reconstructed by employing the recon-all pipeline. In PostFreeSurfer, a brain mask, a cortical ribbon volume image, and cortical myelin maps are generated. Finally, the surface mesh in native space is resampled into fs-LR space[43].

Functional image preprocessing. T2*-weighted functional images were preprocessed in accordance with the resting-state functional processing pipeline of the HCP-D[33,43]. First, volumes were preprocessed using FSL FLIRT to correct for head motion and dynamic distortions[44]. FSL FLIRT was also employed for non-linear alignment to the MNI standard space. Second, distortions in the phase encoding direction were estimated using FSL TOPUP[40]. Third, volumes were resampled from standard space to a surface representation consisting of 91,282 gray matter coordinates. Fourth, gray matter ribbons were determined in native space with the fslmaths tool in FSL and mapped to the gray matter coordinates surface using the Connectome Workbench tool (v1.4.2). Fifth, head motion indices and

independent components were regressed out using FMRIB's ICA-FIX (v.1.0.6.14). In the final step, images were re-registered to the cortical surfaces using MSMAll (v.1.0)[45].

Population connective field modeling analysis

Registration of functional images from volume to surface space. Structural surfaces in native T2-weighted image space were warped into the native volume space of the functional images using the affine transformation matrices generated by dHCP (boundary-based registration, FSL FLIRT). Subsequently, functional volumetric data were projected to the resulting surface using the ribbon-constrained mapping approach implemented in the Connectome Workbench tool (v1.5.0).

Region of interest definition. Regions of interest were primary and secondary visual cortices (V1 and V2) defined by Wang's anatomical template[16]. To be able to examine the internal retinotopic organization of V2, this region was partitioned into three equally sized foveal, middle and peripheral subregions, and into two equally sized dorsal and ventral subregions, in accordance with Benson's template[15]. Following Bock and colleagues[17], eccentricity was estimated in foveal, middle, and peripheral subregions while polar angle was estimated in dorsal and ventral subregions, each of which contained the same number of vertices (see Retinotopic template and projection section below).

Population connective field model estimation. First, hemodynamic time series in each vertex were converted to time series of percent signal change.

$$a_v(t) = \{s_v(t) - mean_v\} \times 100,$$

where, $a_v(t)$ and $s_v(t)$ represent the functional activity in percent signal change and the raw signal of the vertex v at time point t, respectively, and $mean_v$ is a time-averaged raw signal of the vertex v.

Next, candidate connective fields were specified. The cortical connective field for each voxel v in the target region $V2$ consists of weights for each vertex w in the source region $V1$, with w_0 denoting the

center vertex of the connective field in the source region $V1$. Each candidate connective field model is a Gaussian distribution defined by its center vertex w_0 and its spread σ over the cortical surface.

$$g_{w_0,\sigma}(w) = exp(-\frac{d(w_0, w)^2}{2\sigma^2}),$$

where, $d(w_0, w)$ indicates the shortest distance from the center voxel w_0 to all other voxels w in the source region along the cortical surface mesh and $g_{w_0,\sigma}(w)$ indicates the connective field weights for all w, centered on w_0 with a spread σ. Distances between vertices were calculated along the pial surface using a Scipy (v1.12.0) implementation of the Dijkstra algorithm in Python (v3.11.7).

For each connective field g, the weights of the cortical field in the surface mesh were then used to compute a time series. The time series $a_w(t)$ of all vertices w in $V1$ are weighted by their contribution to the cortical field $g_{w_0,\sigma}(w)$ and summed up to constitute the time series of the connective field $c_{w_0,\sigma}(t)$.

$$c_{w_0,\sigma}(t) = \sum_w a_w(t) \cdot g_{w_0,\sigma}(w)$$

The fit of the connective field model was defined as the Pearson correlation between the time series of the connective field and the time series of the V2 vertex. For an initial parameter search, candidate time series of the connective field were calculated for all V1 vertices and 10 cortical spread values between 3 and 25 mm. A non-linear optimization over sigma was performed for all vertices with model fits r > 0.1, using the Broyden-Fletcher-Goldfarb-Shanno algorithm implemented in Scipy's optimization module.

Null model estimation on simulated data. To create a null model without retinotopically organized signals, alternative hemodynamic data on the surface were simulated using a local correlation model. For each surface vertex, a random time series was generated from a normal

distribution with the same number of timepoints as the empirically measured hemodynamic data. The local correlation in V1 and V2 was then smoothed using a Gaussian filter with a kernel width of 30 mm and adjusted to match the median correlation coefficient of the empirical data.

Retinotopic template projection. Retinotopy templates containing eccentricity and polar angle values were derived from adult templates[15 16]. As the templates were defined on the fsaverage surface mesh template in FreeSurfer, it was necessary to warp these templates from fsaverage space to native space. Due to the structural differences between developing and adult brains, a direct transformation from fsaverage to native space could introduce misalignment or distortions. Accordingly, a four-step registration procedure was applied to the retinotopy templates instead, including (1) registration from fsaverage space to the space of the young adult template of the Human Connectome Project (HCP), (2) registration from young adult space to the space of the 40-week template of the dHCP[46] (3) registration from 40-week space to the space of an age-matched group template, and (4) registration from the age-matched group template space to native space.

For the first registration step, we used the registration sphere of the HCP young adult mesh deformed to fsaverage, available from the HCP[43]. For the second registration step, we used an existing sphere generated during the transformation of the dHCP 40-week template sphere to the HCP sphere[29]. For the third registration, we used an existing sphere that was generated in the dHCP by transforming an age-matched template sphere to the 40-week template sphere. For the fourth registration, the native surface sphere was rotated to align with HCP fsLR volumetric space and then registered to the age-matched template sphere of the dHCP using the Biomedical Imaging Analysis Group's Medical Image Restoration Toolkit (MIRTK) and the newMSM software package (v.0.5.1-BETA), following the procedure implemented in https://github.com/ecr05/dHCP_template_alignment. As a final step, these four registrations were concatenated and used to resample the template from

fsaverage space to native space. The transformation and concatenation of all registrations was performed using the Human Connectome Project workbench toolkit (v1.5.0).

As the preprocessed resting-state fMRI data provided by the HCP is resampled in fs-LR space, registration was performed only once from fs-LR to fsaverage space. All remaining analysis steps were identical between the HCP and dHCP data.

Local gradient analysis. To quantitatively assess the direction of change in the V2 polar angle estimates, we computed a gradient at each vertex in a right-to-left, anterior-to-posterior and dorsal-to-ventral coordinate system. A gradient was defined as the sum of the difference between polar angle values of neighboring vertices multiplied by the differences between one vertex and neighboring vertices (vectors) divided by the sum of the squared Euclidean norm of the differences between vectors. If the number of connected vertices of a vertex is *n*, the gradient at vertex *k* is calculated as follows:

$$gradient_k \approx \frac{\sum_{i=1}^{n}(p_i - p_k)(v_i - v_k)}{\sum_{i=1}^{n}\left|\left|v_i - v_k\right|\right|^2}$$

where *p* is the polar angle value of the vertex and *v* is a position vector of the vertex in a three-dimensional real coordinate space $\Re^3$. Averaged gradients were evaluated for each axis and group based on a bootstrapping analysis in which the null hypothesis was that the mean gradient was equal to the bootstrapped mean gradient so that the resulting p-value indicated whether this null hypothesis was confirmed or rejected.

Statistical analyses

Between-group comparison of connective field distributions. To ascertain whether the connective field estimates within each region of interest exhibit differential distributions across age

groups, we employed bootstrapped Kruskal-Wallis tests written in custom Python code. The Kruskal-Wallis test allowed us to determine whether at least one group stochastically dominated at least one other group. Effect size was calculated as the square root of dividing the Kruskal-Wallis test statistic by the number of observations. In the case of significant evidence for stochastic dominance, Mann-Whitney-U tests were performed post hoc for each pair of age groups. The χ^2 value was calculated by randomly resampling the subjects 10,000 times in each group, using the same number of subjects in the original group and allowing duplication using SciPy's *kruskal* function. Effect sizes of Kruskal-Wallis tests were calculated based on the following formula:

$$effect\ size\ (\eta^2) = \frac{H\text{−}statistic - number\ of\ groups + 1}{number\ of\ total\ observation - number\ of\ groups}$$

Mann-Whitney-U tests were carried out to compare pairs of groups post hoc using Scipy's *mannwhitneyu* function. Resulting p-values were family-wise-error corrected. Given that the U statistic follows a z distribution, it was converted to a z score with the following equation:

$$z = \frac{U\ statistic - (n1 \times n2)\ /\ 2}{\sqrt{(n1 * n2 * (n1 + n2 + 1))\ /\ 12}},\ (n1,\ n2:\ number\ of\ observations\ in\ group\ 1\ and\ \ group\ 2)$$

Comparison of connective field modeling results for measured and simulated data. We compared the results of the connective field model applied to the measured fMRI data in the V2 region (1) with the retinotopic values (eccentricity and polar angle) of Benson et al.'s template and (2) with the results of the connective field model applied to simulated fMRI data. For model comparison, we calculated the mean squared difference (MSD).

The following formula was employed to calculate the MSD values:

Measured data vs. Benson template: $MSD_{Benson} = \frac{1}{n}\sum_{i=1}^{n}(p - p_{Benson})^2$,

Measured data vs. Simulated data: $MSD_{Simulated} = \frac{1}{n}\sum_{i=1}^{n}(p - p_{Simulated})^2$.

where n is the number of vertices and p is the connective field parameter value of interest for each vertex. Statistical differences between MSD values were calculated based on Wilcoxon signed-rank tests. Wilcoxon signed-rank tests were performed using Scipy's *wilcoxon* function. Effect sizes of Wilcoxon signed-rank tests were calculated based on z-scores using the following formula:

$$effect\ size\ (r) = \frac{z-score}{\sqrt{number\ of\ observations}}$$

References

1. Himmelberg, M. M., Winawer, J. & Carrasco, M. Polar angle asymmetries in visual perception and neural architecture. *Trends Neurosci.* **46**, 445–458 (2023).
2. Hubel, D. H. & Wiesel, T. N. Uniformity of monkey striate cortex: A parallel relationship between field size, scatter, and magnification factor. *J. Comp. Neurol.* **158**, 295–305 (1974).
3. Tootell, R. B. H., Silverman, M. S., Switkes, E. & De Valois, R. L. Deoxyglucose analysis of retinotopic organization in primate striate cortex. *Science* **218**, 902–904 (1982).
4. Engel, S. A. *et al.* fMRI of human visual cortex. *Nature* **369**, 525–525 (1994).
5. Sereno, M. I. *et al.* Borders of multiple visual areas in humans revealed by functional magnetic resonance imaging. *Science* **268**, 889–893 (1995).
6. Benson, N. C. *et al.* The Human Connectome Project 7 Tesla retinotopy dataset: Description and population receptive field analysis. *J. Vis.* **18**, 23–23 (2018).
7. Himmelberg, M. M. *et al.* Cross-dataset reproducibility of human retinotopic maps. *Neuroimage* **244**, 118609 (2021).
8. Gomez, J., Natu, V., Jeska, B., Barnett, M. & Grill-Spector, K. Development differentially sculpts

receptive fields across early and high-level human visual cortex. *Nat. Commun.* **9**, 1–12 (2018).

9. Dekker, T. M., Schwarzkopf, D. S., de Haas, B., Nardini, M. & Sereno, M. I. Population receptive field tuning properties of visual cortex during childhood. *Dev. Cogn. Neurosci.* **37**, 100614 (2019).
10. Arcaro, M. J. & Livingstone, M. S. A hierarchical, retinotopic proto-organization of the primate visual system at birth. eLife **6**, e26196 (2017).
11. Ellis, C. T. *et al.* Retinotopic organization of visual cortex in human infants. *Neuron* **109**, 2616–2626.e6 (2021).
12. Somerville, L.H. *et al.* The Lifespan Human Connectome Project in Development: A large-scale study of brain connectivity development in 5–21 year olds. *Neuroimage* **183**, 456–468 (2018).
13. Edwards, A. D. *et al.* The Developing Human Connectome Project neonatal data release. *Front. Neurosci.* **16**, 886772 (2022).
14. Haak, K.V. *et al.* Connective field modeling. *Neuroimage* **66**, 376–384 (2013).
15. Benson, N. C., Butt, O. H., Brainard, D. H. & Aguirre, G. K. Correction of distortion in flattened representations of the cortical surface allows prediction of V1-V3 functional organization from anatomy. *PLoS Comput. Biol.* **10**, e1003538 (2014).
16. Wang, L., Mruczek, R. E. B., Arcaro, M. J. & Kastner, S. Probabilistic maps of visual topography in human cortex. *Cereb. Cortex* **25**, 3911–3931 (2015).
17. Bock, A. S. *et al.* Resting-state retinotopic organization in the absence of retinal input and visual experience. *J. Neurosci.* **35**, 12366–12382 (2015).
18. Reid, V. M. *et al.* The Human Fetus Preferentially Engages with Face-like Visual Stimuli. *Curr. Biol.* **27**, 1825–1828.e3 (2017).
19. Donovan, T., Dunn, K., Penman, A., Young, R. J. & Reid, V. M. Fetal eye movements in response to a visual stimulus. *Brain Behav.* **10**, e01676 (2020).

20. Del Giudice, M. Alone in the dark? Modeling the conditions for visual experience in human fetuses. *Dev. Psychobiol.* **53**, 214–219 (2011).

21. Rakic, P. Prenatal genesis of connections subserving ocular dominance in the rhesus monkey. *Nature* **261**, 467–471 (1976).

22. Galli, L. & Maffei, L. Spontaneous impulse activity of rat retinal ganglion cells in prenatal life. *Science* **242**, 90–91 (1988).

23. Katz, L. C. & Shatz, C. J. Synaptic activity and the construction of cortical circuits. *Science* **274**, 1133–1138 (1996).

24. Huberman, A. D., Feller, M. B. & Chapman, B. Mechanisms underlying development of visual maps and receptive fields. *Annu. Rev. Neurosci.* **31**, 479–509 (2008).

25. Himmelberg, M. M. *et al.* Comparing retinotopic maps of children and adults reveals a late-stage change in how V1 samples the visual field. *Nat. Commun.* **14**, 1–15 (2023).

26. Dimitrova, R. *et al.* Preterm birth alters the development of cortical microstructure and morphology at term-equivalent age. *Neuroimage* **243**, 118488 (2021).

27. McIntosh, A. R., Kovacevic, N. & Itier, R. J. Increased brain signal variability accompanies lower behavioral variability in development. *PLoS Comput. Biol.* **4**, e1000106 (2008).

28. Nomi, J. S., Bolt, T. S., Chiemeka Ezie, C. E., Uddin, L. Q. & Heller, A. S. Moment-to-moment BOLD signal variability reflects regional changes in neural flexibility across the lifespan. *J. Neurosci.* **37**, 5539–5548 (2017).

29. Williams, L. Z. J. *et al.* Structural and functional asymmetry of the neonatal cerebral cortex. *Nat. Hum. Behav.* **7**, 942–955 (2023).

30. Carney, O. *et al.* Incidental findings on brain MR imaging of asymptomatic term neonates in the Developing Human Connectome Project. *eClinicalMedicine* **38**, 100984 (2021).

31. Hughes, E. J. *et al.* A dedicated neonatal brain imaging system. *Magn. Reson. Med.* **78**, 794–804 (2017).

32. Fitzgibbon, S. P. *et al.* The developing Human Connectome Project (dHCP) automated resting-state functional processing framework for newborn infants. *Neuroimage* **223**, 117303 (2020).

33. Harms, M. P. *et al.* Extending the Human Connectome Project across ages: Imaging protocols for the Lifespan Development and Aging projects. *Neuroimage* **183**, 972–984 (2018).

34. Makropoulos, A. *et al.* The developing human connectome project: A minimal processing pipeline for neonatal cortical surface reconstruction. *Neuroimage* **173**, 88–112 (2018).

35. Cordero-Grande, L., Hughes, E. J., Hutter, J., Price, A. N. & Hajnal, J. V. Three-dimensional motion corrected sensitivity encoding reconstruction for multi-shot multi-slice MRI: Application to neonatal brain imaging. *Magn. Reson. Med.* **79**, 1365–1376 (2018).

36. Kuklisova-Murgasova, M., Quaghebeur, G., Rutherford, M. A., Hajnal, J. V. & Schnabel, J. A. Reconstruction of fetal brain MRI with intensity matching and complete outlier removal. *Med. Image Anal.* **16**, 1550–1564 (2012).

37. Tustison, N. J. *et al.* N4ITK: improved N3 bias correction. *IEEE Trans. Med. Imaging* **29**, 1310–1320 (2010).

38. Smith, S. M. Fast robust automated brain extraction. *Hum. Brain Mapp.* **17**, 143–155 (2002).

39. Makropoulos, A. *et al.* Automatic whole brain MRI segmentation of the developing neonatal brain. *IEEE Trans. Med. Imaging* **33**, 1818–1831 (2014).

40. Andersson, J. L. R., Skare, S. & Ashburner, J. How to correct susceptibility distortions in spin-echo echo-planar images: application to diffusion tensor imaging. *Neuroimage* **20**, 870–888 (2003).

41. Andersson, J. L. R. *et al.* Towards a comprehensive framework for movement and distortion

correction of diffusion MR images: Within volume movement. *Neuroimage* **152**, 450–466 (2017).

42. Salimi-Khorshidi, G. *et al.* Automatic denoising of functional MRI data: combining independent component analysis and hierarchical fusion of classifiers. *Neuroimage* **90**, 449–468 (2014).
43. Glasser, M. F. *et al.* The minimal preprocessing pipelines for the Human Connectome Project. *Neuroimage* **80**, 105–124 (2013).
44. Jenkinson, M., Bannister, P., Brady, M. & Smith, S. Improved optimization for the robust and accurate linear registration and motion correction of brain images. *Neuroimage* **17**, 825–841 (2002).
45. Glasser, M. F. *et al.* A multi-modal parcellation of human cerebral cortex. *Nature* **536**, 171–178 (2016).
46. Bozek, J. *et al.* Construction of a neonatal cortical surface atlas using Multimodal Surface Matching in the Developing Human Connectome Project. *Neuroimage* **179**, 11–29 (2018).

Data availability

The data for this study are available after institutional registration through public links in the National Institute of Mental Health Data Archive (NDA). Prenatal and neonatal data are available at https://nda.nih.gov/edit_collection.html?id=3955. Adolescent and adult data are available at https://nda.nih.gov/edit_collection.html?id=2846.

Code availability

All data analysis was performed with custom software using Python 3.11 and various third-party packages (matplotlib 3.8.3, numpy 1.26.3, pandas 2.2.0, scipy 1.12.0, and nibabel 5.2.0). Brain surfaces were visualized with nilearn (0.10.4). All code used for data analysis is available from GitHub (https://github.com/SkeideLab/SPOT).

Acknowledgements

This work was supported by the German Research Foundation (DFG Heisenberg Program Grant 433758790 awarded to M.A.S.), the Alexander von Humboldt Foundation (M.A.S. was appointed to the Henriette Herz Scouting Programme) and the Jacobs Foundation (Research Fellowship awarded to M.A.S.). Data were provided by the developing Human Connectome Project, KCL-Imperial-Oxford Consortium funded by the European Research Council under the European Union Seventh Framework Programme (FP/2007-2013) / ERC Grant Agreement no. [319456]. We are grateful to the families who generously supported this study.

Author contributions

M.A.S. conceived the study. S.Y. and A.K. analyzed the data. S.Y. visualized the results with feedback from A.K. and M.A.S. S.Y. and M.A.S. wrote the manuscript with feedback from A.K. M.A.S. supervised the study.

Ethics declarations

The authors declare no competing interests.